JMEPEG (2011) 20:719–730
DOI: 10.1007/s11665-010-9797-8

1059-9495/$19.00

Finite-Element Simulation of the Anti-Buckling-Effect of a Shape Memory Alloy Bar

Frank Richter, Oliver Kastner, and Gunther Eggeler

(Submitted May 14, 2010; in revised form October 20, 2010)

Shape memory alloys (SMA) are characterized by an intricate stress-strain curve modified by temperature, posing thermomechanically coupled problems. A model able to address this feature is the Müller-Achenbach-Seelecke (MAS) model which had been ported into the user material interface in the finite-element (FEM) simulation software ABAQUS. The literature on this model mainly focuses on pseudo-elasticity of SMA at elevated temperature. We address a numerical investigation in the low-temperature pseudo-plastic regime. The present publication deals with the little-known anti-buckling effect which occurs in de-twinned and pre-bent martensitic bars under axial compression. It was experimentally demonstrated by Urushiyama et al. (JSME (The Japan Society of Mechanical Engineers) Int. J. Ser. A, Solid Mech. Mater. Eng., 2003, 46(1), p 60-67). This study reveals that the origin of this effect roots in an interplay of inhomogeneous stress states and mechanically induced twin-twin phase transformations. The proper explanation of the anti-buckling effect can be inferred from the explicit knowledge of the martensitic phase composition of the bar during the process. We show that the MAS model is capable to resolve this matter in detail, hence addressing the reliability of this particular model also in the pseudo-plastic regime of SMA. The study thereby implies that the MAS model is an excellent modeling tool for the analysis of complex, thermomechanically coupled processes.

Keywords advanced characterization, mechanical testing, modeling processes

1. Introduction

Shape memory alloys (SMA) are an intriguing class of materials that feature intricate thermomechanical interplay of the phases present in a SMA, austenite and martensite. As phase transformations between the constituent phases can be induced by either stress or temperature, their stress-strain curves depend strongly on temperature and the mechanical behavior can be broadly classified in pseudoplasticity (at low temperature) and pseudoelasticity (at high temperature).

Various theoretical models were elaborated to address SMA behavior. Results obtained for typical load cases can be used to assess the capability of these models for predicting the response of SMA in critical usage, such as sensors and actuators. Evidently, models are more likely to yield results close to experimental data if they incorporate actual physical phenomena. The physics behind SMA are accentuated by the occurrence of latent heat either emitted or absorbed whenever phase changes are initiated, giving rise to concurrent modification of material parameters. From the martensitic state, the supply of heat may trigger the shape-memory effect which renders SMA attractive in actuation devices. Often, such machine parts are critical and hence a thorough understanding of their behavior when exposed to thermal and mechanical loads is required for prediction of their performance. Hence, a model suitable for SMA must be able to solve mechanical and thermal equations simultaneously.

The model used here relies on free energy functions derived by the use of statistical thermodynamics for crystallographic elements considered to be thermally activated. Transformations may be induced either thermally or athermally by application of loads. Latent heat effects are incorporated in a natural way. This characteristic of its physical representation renders the full thermomechanical coupling a key feature of the model named after Müller, Achenbach, and Seelecke (henceforth MAS model). The physics of the model and its achievements in numerics reported so far are concisely reviewed in section 2.

The present work adds the little-known anti-buckling effect (section 3) to the range of loading scenarios that can be mastered by the MAS model. This effect renders SMA bars resistant to buckling as a sideways deflection can be reversed by an axial force. It was reported that a SMA bar, detwinned so as to orientate the martensite and bent, straightens when exposed to an axial compressive load (Ref 1, 2). A numerical treatment of this amazing effect has already been carried out by the original authors (Ref 1), but the finite-element simulation discussed here (sections 4-6) offers far more insight. The temporal and spatial variation of stresses and phase fractions are discussed. A formula augmenting the commonplace interrelationship between bending moment and stress by a phase-fraction-dependent term achieves an interpretation of the anti-buckling effect and is corroborated by direct FEM output.

This article was a poster at Shape Memory and Superelastic Technologies 2010, held May 16-20, 2010, in Pacific Grove, California, and has been expanded from the original presentation.

Frank Richter, Oliver Kastner, and **Gunther Eggeler**, Institute of Materials, Ruhr-University Bochum, Bochum, Germany. Contact e-mail: Oliver.Kastner@rub.de.

2. The MAS Model and its FEM Implementation in General

Crystallographic observations reveal that SMA exhibit a layered crystalline structure. The MAS model rationalizes this observation by considering ideal mesoscopic crystal layers in one of the three model phases austenite (A) and two martensitic twin phases ($M+$, $M-$) (Ref 3-11). The model derivation adheres strictly to thermodynamics and roots in the idea of a three-well potential energy with minima indicating the stable locations of these three phases. The model yields a constitutive equation for the stress σ as a function of external strain ε and the internal variables x_A, x_{M+}, and x_{M-} which express the phase fractions of the model phases,

$$\sigma = \frac{\varepsilon - (x_{M+} - x_{M-}) \cdot \varepsilon_T}{\frac{x_{M+}}{E_M} + \frac{x_{M-}}{E_M} + \frac{x_A}{E_A}}. \quad \text{(Eq 1)}$$

The elasticity of the pure phases is expressed by the Young's moduli E_M and E_A and a martensitic transformation causes a residual strain ε_T. According to the MAS model, the phase fractions are implicitly functions of the temporal evolution of the stress-strain field and the temperature. These are determined by a set of rate equations representing an initial value problem (coupled ODE system) that can be solved numerically for given strain and temperature,

$$\begin{aligned} \dot{x}_{M+} &= -p_{+A} \cdot x_{M+} + p_{A+} \cdot x_A \\ \dot{x}_{M-} &= -p_{-A} \cdot x_{M-} + p_{A-} \cdot x_A \,. \\ 0 &= \dot{x}_A + \dot{x}_{M-} + \dot{x}_{M-} \end{aligned} \quad \text{(Eq 2)}$$

Herein, the p are the transition probabilities with subscripts indicating the transition direction. This coupled ODE set is numerically stiff and requires a stable integration scheme for robust solution. We use an implicit Runge-Kutta scheme of order five with an adaptive time step size called RADAU IIa (Ref 12). The temperature evolution within the specimen is due to latent heat emission and absorption and the according heat exchange with the ambiance. Assuming temperature homogeneity in simple geometries, the temperature can be calculated from the integral energy balance which represents an additional differential equation to be solved along with the rate equations for the phase fractions. Previously, this was accomplished by a standalone FORTRAN program (Ref 7, 10, 13).

ABAQUS/Standard allows user implementations of constitutive equations of state through a FORTRAN subroutine called User Material (UMAT) where the state of the nodal field quantities (here: displacements and temperature) can be accessed. UMAT is called by ABAQUS within its own numerical procedure while striving for a converged solution. We have used the UMAT interface to adopt the standalone implementation of the MAS model into the ABAQUS environment. Further, the user has to provide the Jacobian stiffness matrix which for the MAS model reads

$$\frac{\partial \Delta\sigma}{\partial \Delta\varepsilon} = \frac{\partial \sigma}{\partial \varepsilon} + \frac{\partial \sigma}{\partial x_{M+}} \cdot \frac{\mathrm{d}x_{M+}}{\mathrm{d}t} \cdot \frac{\mathrm{d}t}{\mathrm{d}\varepsilon} + \frac{\partial \sigma}{\partial x_{M-}} \cdot \frac{\mathrm{d}x_{M-}}{\mathrm{d}t} \cdot \frac{\mathrm{d}t}{\mathrm{d}\varepsilon} \quad \text{(Eq 3)}$$

owing to the dependence of the phase fractions on time t and the identity $x_A = 1 - (x_{M+} + x_{M-})$ (Ref 14, 15) while ε_T is a constant. The relevant material data and numerical parameters are given in Table 1.

The references given above have provided ample justification for stating that the MAS model has potential for efficient simulations of SMA behavior. The MAS model in its present uniaxial formulation restricts applicable load scenarios to those where uniaxial stress dominates such as loading in wires and trusses (Ref 14) as well as pure beam bending (Ref 15) and pure torsion (Ref 16, 17). The most recent progress devoted to this model was its implementation in the finite-element-program (FEM) ABAQUS™ (Dassault Systèmes Simulia Corp., Providence, RI, USA), producing data consistent with reference data for both pseudoelastic and quasiplastic settings (Ref 18). Recently, the simulation of a shrink-fit (Ref 19) expanded the wealth of options for the MAS model which also addresses polycrystalline materials (Ref 16, 20, 21). Arbitrary, multiaxial stress/strain states can be addressed by the use of multivariant extension of the MAS model in principle (Ref 22). The FEM implementation of such an augmented model is an ongoing task.

3. Anti-Buckling

This section provides a concise description of the individual loading steps detailed in the original work (Ref 1, 2). In the following discussion, we refer to the three loading stages I-III sketched in Fig. 1. Stages I and II indicate the experimental preparation of a pseudoplastic SMA bar by detwinning under

Table 1 Model parameters of the FEM/MAS simulation

Symbol	Value	Unit	Physical interpretation
MAS model parameters (Ref 14, 15)			
E_A	71.1	GPa	Young's modulus of austenite
E_M	30.9	GPa	Young's modulus of martensite
ε_T	0.044	1	Transformation strain of martensite
V_{act}	5×10^{-23}	m^3	Activation volume
ρ	6500	kg/m^3	Density
Geometrical parameters			
l_0	50	mm	Length of SMA bar
D	4.38	mm	Edge length of SMA bar (square cross section)
Numerical parameters			
atol, rtol	10^{-14}	1	Tolerances in RADAU algorithm
STABILIZE	5×10^{-5}	1	Parameter for STABILIZE command in ABAQUS, denoting the dissipated energy fraction of the automatic damping algorithm within automatic stabilization

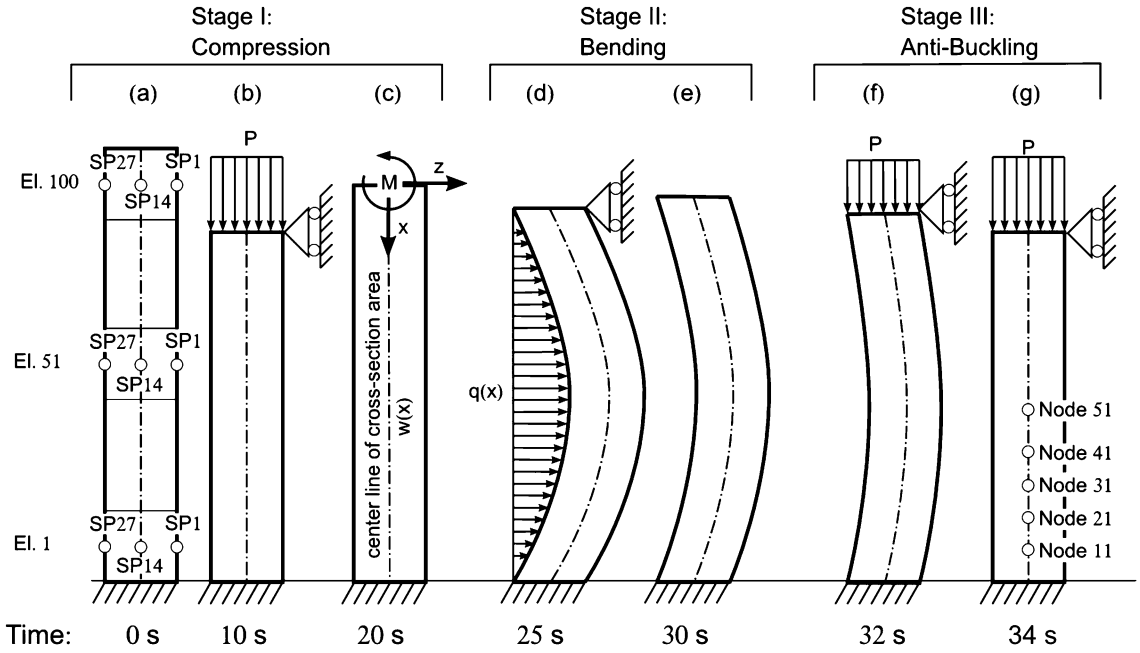

Fig. 1 Sketch of three loading stages applied to a pseudo-plastic SMA bar to produce the anti-buckling effect. The indicated instants on the timeline refer to the simulation only. Note that in stage II, the original authors employ three-point bending in their experiment. Here, the side deflection is modeled here by a lateral load $q(x)$

compressive load (I) and by side deflection (II). The thus prepared bar is able to display the anti-buckling effect during final axial compression in stage III. We summarize the original experiment (Ref 1) in the following:

I. A straight bar made of the SMA Ti-Ni-Cu is axially compressed below the austenite start temperature. In the as-received initial state, the unloaded bar is a phase mixture of martensite variants. An axial compressive load exceeding the martensite-martensite transformation load causes load-induced martensite-martensite transformations into that martensite variant favored by compression. This process is labeled "de-twinning". It is accompanied by small, remanent deformation according to the transformation strain caused by the de-twinning process and prevails upon unloading. After complete load relief the bar remains slightly shortened and is entirely composed of the martensite variant favored by compressive axial load.

II. Subsequently, the bar is exposed to three-point bending by a force acting perpendicularly to the bar axis. Such lateral loading causes an inhomogeneous stress distribution across the bar cross section: bar fibers located on the loading side ("inner fibers") are compressed, while the fibers on the opposite side ("outer fibers") are stretched. Eventually, the stress level in the outer fibers exceeds the martensite-martensite transformation stress, inducing pseudo-plastic deformations and effect significant transformation strains. Upon unloading, these transformations are not reverted and the sample remains deflected after complete removal of the external load.

III. The pre-bent bar is exposed to an axial compressive load again. In this setting, the pseudo-plastic SMA does not buckle as expected for an ordinary material, rather the deflection is gradually decreased and eventually completely reverted during loading. This anti-intuitive behavior roots in the fact that pseudo-plasticity, in contrast to regular plasticity, is based on revertible lattice transformations between martensite variants and is not caused by plastic lattice destruction. This fact is expressed by the particular nonlinear stress-strain interdependence of SMA. Final unloading of the straightened bar eventually produces the de-twinned configuration of load stage I.

Heating effects observed during the process (Ref 1) are minor and the temperature always rests below the austenite start temperature. Thus, the phenomena are restricted to the pseudoplastic material regime. Because the anti-buckling effect refers to re-orientations of martensite, the effect is also called the "twinning deformation effect." The original authors contribute a theoretical analysis to their experimental findings which may serve as reference solution for the numerical study described here. Appropriate reference to their findings will be made throughout the manuscript.

4. Modeling of the Anti-Buckling Effect

4.1 FEM Model

The FEM model of the process is taken as geometrically linear and employs the ABAQUS beam element B23. It mimics the classical beam analysis and can be applied in situations where normal stresses prevail during loading. The fundamental idea is that loading effects normal stresses in hypothetical material fibers along the beam axis. The beam elements B23 features three integration points along the length and allow evaluating the fiber stress states at discrete section points (SP) across the beam cross section. Using this model, the bar is

discretized into 100 elements bottom-up along the bar axis as shown in Fig. 1 (0 s). Each element has 27 SP located equidistantly across the cross-sectional area. SP1 represents the outermost fiber and SP27 the innermost one in the direction of lateral load application (described subsequently). The 100 beam elements are spanned by 101 nodes subjected to mechanical boundary conditions. The bottom node (node 1) is fixed in time and space and the top node (node 101) is the loading point to induce compressive forces in the load stages I and III. The latter is restricted to axial movement. All the remaining nodes 2-100 are free to move in the plane of the sketch. Rotatory degrees of freedom are allowed for all nodes. The dimensions of the sample are given in Table 1.

4.2 Model Restrictions

Since the original authors do not provide all the thermomechanical properties of the specific SMA used in the experiment we assume a "suitable" set of material parameters. The set used with this study is taken from (Ref 14, 15) and is documented in Table 1. While the original work considers poly-crystalline SMA, the model used here is restricted to a single-crystalline sample. Thus, the clarity in localizing stress profiles within the bar is enhanced as the transformation stress is unaltered while transforming. As of now, a poly-crystalline version of the MAS model exists only for pseudo-elastic SMA (Ref 20, 21). The complete stress-strain relation produced by the MAS model at the reference temperature (273 K) is shown in Fig. 2. Note that during the entire process here, only a part of this curve is accessed by the bar (Fig. 5, described below). Another model restriction arises from the fact that ABAQUS beam elements are strictly mechanical elements, i.e., they feature no temperature degree of freedom, limiting the simulation to an isothermal situation (273 K). As latent heat effects are minor in the pseudo-plastic regime, however, this restriction is uncritical. Latent heat effects become important in pseudo-elastic SMA which are not considered here.

As a consequence of these restrictions, the results cannot be compared to the experiment quantitatively, rather they explain the effect in a qualitative way. We show that despite the restrictions the MAS model is capable of revealing the fundamental physical effects behind the phenomenon of anti-buckling.

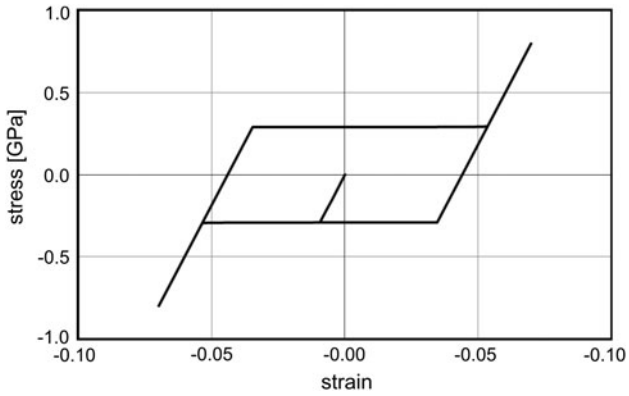

Fig. 2 Stress-strain curve produced by the MAS model for the parameters of Table 1. Reference temperature 273 K

4.3 Simulated Process

In the simulation, the loading history is split into three stages according to Fig. 1. The simulation is performed in a quasi-static setting, where all temporal changes result from time-depending boundary conditions and inertia is neglected. The simulation time scale used here renders model-inherent relaxation times uncritical. The total simulation time is 40 s. For orientation, we provide a brief overview of the simulation process in Table 2 and discuss the results in detail throughout the next sections. Element output quantities were read out from the ABAQUS output database for elements 1 to 96 in increments of five elements and for element 100 (cf. Fig. 7, A1).

Table 2 Overview of the simulation process

Stage I: De-twinning	
0 to 10 s	Axial loading in displacement control mode up to a maximum strain of $-1.5 \cdot \varepsilon_T$. Maximum compressive stress approx. 6.8×10^8 Pa
10 to 20 s	Axial unloading so as to arrive in the stress-free and de-twinned state. Final (strain/stress) = ($-\varepsilon_T$/0.0). The final vertical position of the bar center (node 51) is $\frac{1}{2} \cdot l_0 \cdot (1 - \varepsilon_T) = 0.0239$ m
Stage II: Pre-bending	
20 to 25 s	Lateral loading. The bending of the bar is effected by a cosine-shaped lateral line load, defined as a concentrated contact force $q(n, t)$ along the length according to $q(n,t) = -15 \cdot \frac{1}{c}\left(1 - \left\lvert\frac{t-25\,\mathrm{s}}{5\,\mathrm{s}}\right\rvert\right) \cdot \cos\left(\frac{\pi}{100} \cdot (n - 51)\right) N$ where c is the characteristic element length ($c = 5 \times 10^{-4}$ m) and n is the node number. Note: the factor c is automatically provided by ABAQUS. It is inserted in the above equation to keep the correct dimensions of the contact force (N/m). Further, it is required for comparison of FEM data with analytical results
25 to 30 s	Lateral unloading, linear in time according to $q(n, t)$. Once the load is relieved, the bar remains bent with a maximum deflection of 2.839 mm at the center node
Stage III: Anti-buckling	
30 to 35 s	Axial compression in load control, linear in time, up to a maximum load of −8 kN. The loading quickly triggers the anti-buckling effect. After 33.7 s the straight shape is restored. This step necessitates the ABAQUS command STABILIZE which activates automatic stabilization to alleviate local instabilities. The "dissipated energy fraction" parameter is set to 5×10^{-5}
35 to 40 s	Load reversal, linear in time, unloads the straightened bar elastically

5. Results

In this section, we discuss the simulation results in detail and refer to Fig. 3 to 8 which illustrate the process in various process diagrams: Fig. 3(a), (b) shows the stress history for all SP along integration point 1 of the element 51, which is located at the bar center. Figure 4 provides the history of the phase composition showing the $M+$ fraction (favored by tensile stress) at the same location as function of time focussing on the time interval of 20 to 35 s. Figure 5 shows the process in the stress/strain diagram for that same location. The history of the side deflection of the bar center line is shown in Fig. 6. Figure 7 illustrates the position of the neutral fiber along the bar at four selected instants.

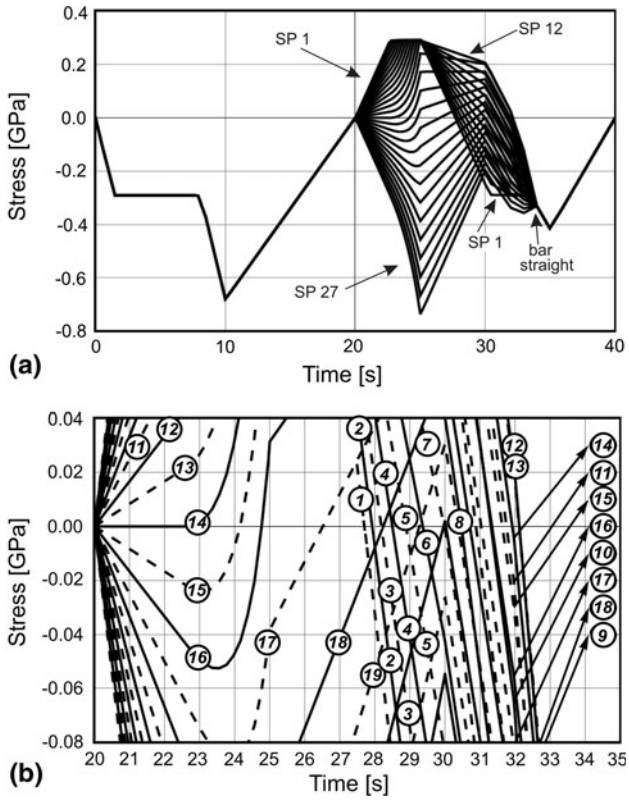

Fig. 3 Stress history at the bar center (element 51, integration point 1) for all SP (1 to 27) across the cross-sectional area. (a) Entire loading history (0 to 40 s), outermost SPs are labeled. (b) Magnification of the inhomogeneous part (20 to 35 s). Plotmarkers indicate section point numbers (not all are labeled for clarity of visualization). SP even: full line; SP odd: dashed line. The crossing of stress-time curves in stage III is illustrated by the data for $t = 32$ s

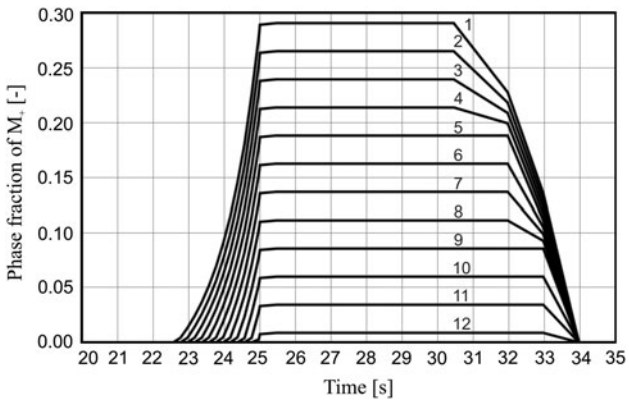

Fig. 4 History of the $M+$ fraction at the bar center (element 51, integration point 1) for all SP (1 to 27) across the cross-sectional area. Plotmarkers (only shown for SP1 to SP12) indicate section point numbers. The representation focuses on the inhomogeneous part (20 to 35 s)

5.1 Stage I

In the initial configuration, the material is characterized by equal amounts of the model variants $M+$ and $M-$. During the

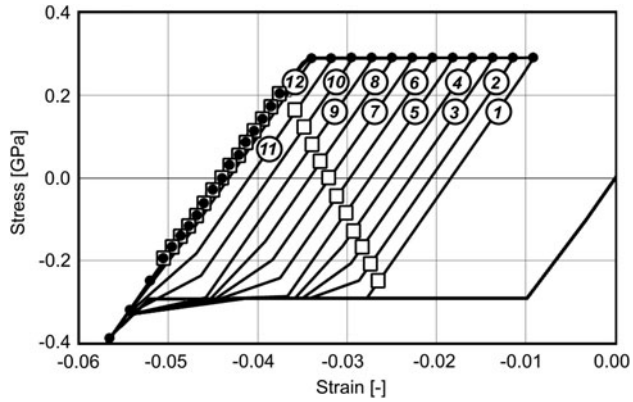

Fig. 5 Stress/strain process diagram. Stress-strain-states at the bar center (element 51, integration point 1) for all SP (1 to 27) across the cross-sectional area. Plotmarkers (only shown for SP1 to SP12) indicate section point numbers. During stages II and III the SP13-SP27 are restricted to move along the leftmost elastic line. Bullets: all SP at the instant of maximum lateral load (25 s), squares: all SP at the end of stage II (30 s, twofold zero crossing). Note: unloading is elastic also in stage III up to merging onto the reverse martensitic transformation horizontal. The bilinear lines within the hysteresis loop and lines that seemingly cross the negative stress horizonal towards the leftmost elastic branch without undergoing transformation are not physical; they are a consequence of selecting only a limited amount of data points in the analysis

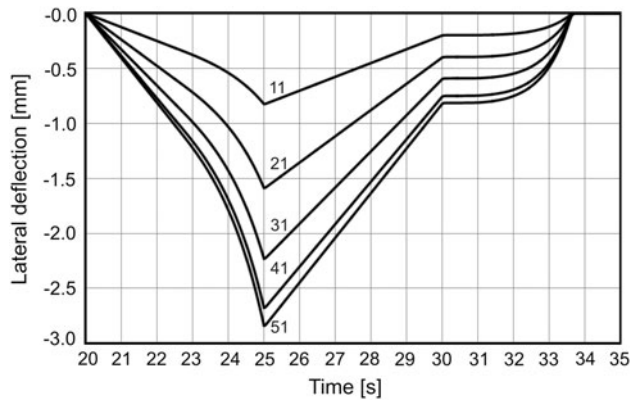

Fig. 6 History of the side deflection at various positions along the bar axis: nodes 11 to 51, node increment 10 (cf. Fig. 1). No side deflection occurs within stage I, therefore this time interval is omitted. At approximately 33.7 s (stage III) the deflection is completely reverted due to the axial load applied

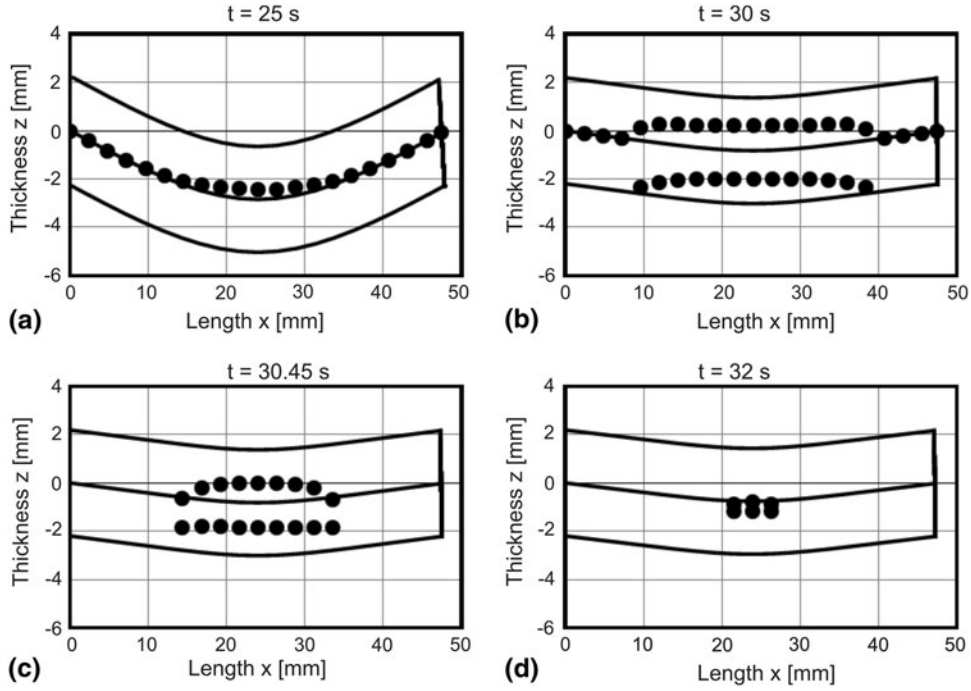

Fig. 7 Location the neutral fiber(s) at the indicated four time instants. Solid, black lines indicate the outer shape (SP1, SP27) and the geometrical center line (SP14). Dots indicate zero stress locations (interpolated between SP)

first 10 s the compressive load is increased by displacing the top node downwards up to a maximum strain of $-1.5 \cdot \varepsilon_T$. The global load response is shown in Fig. 3(a) and is a direct consequence of the load-strain curve in Fig. 2. For small displacements this response is linear and the phase composition is stable, before the transformation stress plateau of −0.29 GPa is entered at 1.5 s of simulation time.

Limiting Eq 1 to the pseudoplastic state where $x_A = 0$ and observing the identity $1 = x_{M+} + x_{M-}$, Eq 1 simplifies to

$$\sigma = E_M \cdot (\varepsilon - (2 \cdot x_{M+} - 1) \cdot \varepsilon_T). \quad \text{(Eq 4)}$$

Fixing the stress to the value of the positive transformation stress reveals that the *M*+ fraction grows linearly with strain along the positive stress horizontal. Likewise, a linear correlation between stress and strain is enforced at constant *M*+ fraction, implying martensite elasticity during unloading prior to any retransformation. Therefore, compressive straining provokes reorientation of the unfavored martensite variant *M*+ into the favored variant *M*−. This process lasts from 1.5 to 7.9 s and changes the *M*− fraction gradually from 0.5 to 1.0. Further compressive straining of the de-twinned bar effects linear compression up to a maximum compressive stress at 0.68 GPa (10 s). At this instant the simulation switches into load relief mode and the compressive load is linearly decreased to zero.

In the stress/strain diagram of Fig. 5, the stage I process starts at the origin, follows the elastic branch of the initial phase mixture towards the compressive (negative) transformation stress, transforms at constant load and eventually returns into the unloaded state along the lateral elastic branch which indicates a pure *M*− state. In the final state of this stage, the bar has undergone a compressive transformation strain of $-\varepsilon_T$. Throughout stage I, all process quantities (stress, strain, composition) change homogeneously within the bar volume.

5.2 Stage II

Subsequently, the bar is laterally loaded (20 to 25 s) and unloaded (25 to 30 s). Instantaneously, the process quantities become inhomogeneous. Side deflection provokes compressive stress states in inner fibers and tensile stresses in outer ones. The largest stresses develop at mid-length of the bar which is represented by integration point 1 of the center element 51. The stress history of all SP at this axial position is shown in Fig. 3. Inspection shows the intricate stress state across the cross-sectional area in this load stage once the tensile transformation stress is exceeded (22.8 s). Below this transformation stress level, the stress distribution is linear and the neutral fiber is located at the geometrical center line of the cross-sectional area (SP14) according to the classical solution for elastic bars. Likewise, Fig. 4 shows the resulting development of the phase fraction *M*+ for all SP at this location. At 22.8 s, the stress on the outermost fiber (SP1) attains the positive transformation stress plateau (0.29 GPa) and initiates partial conversion of *M*− to *M*+ (Fig. 4). For fibers approaching the center line (i.e., higher SP numbers), this instant is delayed, while from SP13 onwards the stress remains always below the transformation stress, hence no transformations evolve in these regions. On the inner side, fibers are exposed to a rising magnitude of compressive stress. In contrast to the outer fibers, the inner fibers (being completely in the *M*− phase) experience pure elastic compression according to the stress-strain relation of the model material of Fig. 2. Note the model disregards any plastic deformation of martensite at larger stress intensities. Consequently, the stress profile becomes asymmetric with respect to the geometrical center (Fig. 3). While the tensile stresses are limited by the transformation stress plateau during stage II, compressive stresses increase without bound dictated by the bar deflection. Consequently, the neutral fiber is shifted off the geometrical center line towards the compression side

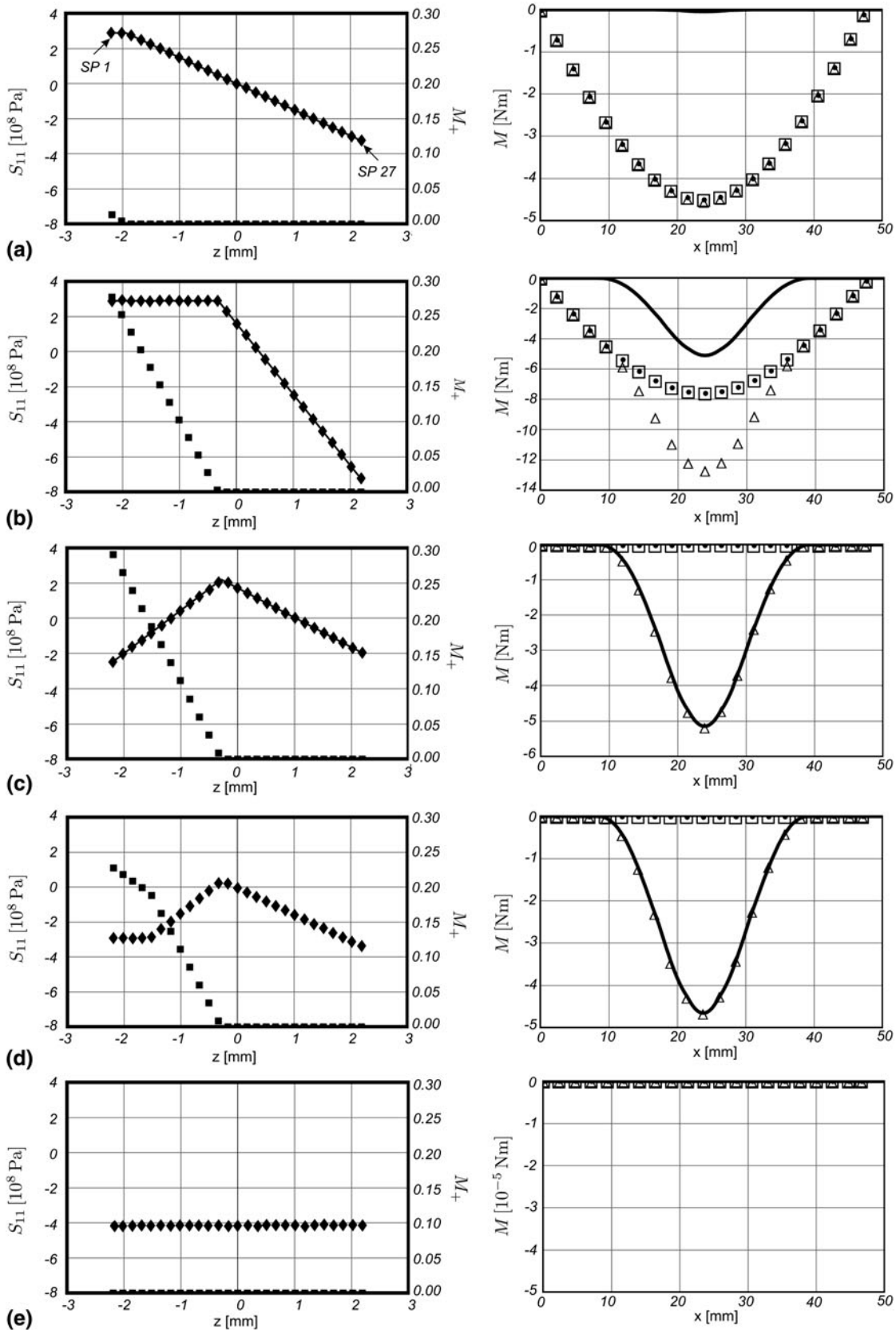

Fig. 8 State diagrams at the instants of 23 (a), 25 (b), 30 (c), 32 (d), and 35 s (e). Left column: stress distribution and the distribution of the $M+$ fraction across the bar thickness at mid-length (node 51, integration point 1). Ordinate axis: stresses refer to the left ordinate, phase fractions to the right ordinate. The solutions obtained for the SMA material are plotted by symbols (stresses: diamonds, phase fraction: squares). Diagrams a, b, and c also incorporate the stress for a modified Prandtl-Reuss body. Right column: bending moment diagrams along the bar axis (Eq 7). Hollow triangles: $M_{el}(x)$, solid black line: $M_{tr}(x)$, squares: $M_{el}(x) - M_{tr}(x)$, bullets: reference data SM1 provided by ABAQUS

(i.e., to higher SP numbers). This is first detectable at approximately 22.8 s (Fig. 3b), when the geometric center line (located at SP14) is no longer stress-free.

During unloading (25 to 30 s), the asymmetry of the stress profile affects a bifurcation of the neutral fiber into two lateral branches in those regions of the bar which experienced transformations during prior deflection. Prior to removing the external contact load the tensile stresses in the outer transforming fibers (bullets on positive stress horizontal in Fig. 5) are balanced with respect to the compressive stresses in the inner fibers. Since the latter are larger in magnitude (note that the five inner SP have stress values below −400 MPa in Fig. 3 at $t = 25$ s) than the tensile stresses on the outer side, the relaxation process is accompanied by a contraction of the outermost fibers in the transformed region while the inner fibers relax. This slight contraction, however, is not sufficient to revert the transformation in the outer fibers. Therefore, a bending moment is preserved, which causes a remanent deflection of the bar even upon complete removal of the external load. Consequently, a complex stress state is produced at the end of this load stage at 30 s, characterized by the occurrence of two neutral fibers displaced from the geometrical center line (see Fig. 5 for the central element and Fig. 7 for the entire specimen length).

It is instructive to discuss the stage II process in the stress/strain diagram of Fig. 5. Out of the 27 SP, the outer 12 ones experience $M-$ to $M+$ transformations during deflection (Fig. 3a-5). At maximum lateral load (25 s, full circles in Fig. 5), the state points of these outer 12 fibers are located on the tensile stress plateau according to their local martensite composition. At this instant, the outermost fiber (SP1) has produced the largest amount of $M+$ (29%) and has achieved a local strain of approximately −1%. The next fiber SP2 has experienced the transformation stress slightly later; therefore, the $M+$ fraction is smaller and the local transformation strain is larger by magnitude. Going from SP1 to SP12, the $M+$ fraction decreases and the magnitude of the local transformation strains increases. Release of the external load (after 25 s) relieves the tensile stresses in the outer fibers SP1-SP12, while their composition is preserved. Therefore, the process states of these 12 fibers move along their individual elastic branches into the hysteresis loop of the stress/strain curve. Inner fibers, which are compressed during the bending and therefore not affected by transformations, find new equilibrium positions along the leftmost elastic branch of the curve in Fig. 5. In the final state of load stage II, the fiber states populate the diagram according to their individual conditions (squares in Fig. 5), which are obviously inhomogeneous.

Figure 6 shows the progress of the deflection for selected nodes along the bar axis within the time interval of 20 to 35 s. The location of these nodes is indicated in Fig. 1 (34 s). This representation illustrates how the deflection is built up during loading (20 to 25 s) with a maximum deflection of 2.839 mm at the mid-length (node 51). At this position, a remanent deflection of approximately 0.82 mm prevails after complete external unloading (30 s).

5.3 Stage III

The complex mechanical equilibrium in the partially transformed bar produced by the previous load stages is now superimposed by an axial compressive load. Since the geometric center line of the bar is bent, such axial compression produces a slight bending moment, provoking a buckling instability in an ordinary material. In the SMA bar, however, the axial loading superimposes onto the intricate stress state and shifts the stress state of fibers previously transformed onto the compressive transformation plateau along which they finally merge with the state of fibers not affected by transformations. Consequently, previously transformed fibers gradually retransform into the $M-$ phase. This process simultaneously reduces the bending moment, straightening the bar. The progress of this process is clearly visible in Fig. 3(b) and 4. The onset of the re-transformation is at 30.45 s in the outermost fiber SP1. The stress values below the negative stress horizontal attained between this instant and the complete straightening of the bar in Fig. 3 refer exclusively to section points that did not experience the $M-$ to $M+$ transformation. Recall that pure elasticity prevails in these layers. Finally, after approximately 33.7 s, all previously transformed fibers SP1-SP12 have converged to the compressive transformation stress. Consequently, they are shifted along that plateau to the inflection point in the stress-strain curve, and the bar is composed of pure $M-$. The stress state remains nonuniform until the bar deflection has completely vanished at approximately 33.7 s. From this instant onwards all volume elements follow a unique line in Fig. 3(a) again.

The anti-buckling process is also indicated by the history of the side deflection shown in Fig. 6. At the bar mid-length (node 51), a deflection of ca. 0.82 mm (30 s) is completely recovered during the axial loading of stage III. The same behavior is exhibited at other locations along the bar axis (nodes 11, 21, 31, and 41, Fig. 1). Eventually, after 33.7 s, all nodes merge onto the center line of the undisturbed configuration and the straight bar shape is recovered.

Stage III can also be discussed with the aid of Fig. 5. The final state of the previous stage II was indicated by an inhomogeneous stress/strain/composition state where all fibers have occupied individual equilibrium states, with the outer fibers being affected by phase transformations (squares in Fig. 5). In this situation, external axial compression shifts the local stress state of these fibers towards the compressive transformation stress plateau. This critical load is first experienced by the outmost fiber SP1, which is located closest to this limit at the end of stage II, followed by the remaining fibers SP2-SP12 as the external compression is continued.

5.4 Neutral Fiber

Owing to the nonlinear character of the stress/strain relation, the stress distribution across the bar becomes asymmetric during load stage II (20 to 30 s). As a consequence, the location of zero stress (the neutral fiber) is shifted off the geometrical center line. Figure 7 shows plots of the location of the neutral fiber(s) across the bar section. Lateral loading effects a deviation of the neutral fiber (indicated by black bullets) from the geometrical center line (central solid line) in those parts of the bar where the tensile stress exceeds the transformation stress in outer fibers (Fig. 7, 25 s). During removal of the lateral contact load, the outer fibers, which experienced transformations during loading, are balanced in favor of stress relaxation of the inner, compressed fibers. This situation provokes a bifurcation of the neutral fiber into two lateral branches visible in Fig. 5 and 7 at 30 s. Axial loading in stage III affects shortening of these two branches as the transformation in the outer fibers is reverted (Fig. 7, 30.45 s). As the bar straightens

under compression, the two branches approach the bar center (Fig. 7, 32 s). Finally, the entire volume of the bar is subjected to compressive stresses and a neutral fiber no longer exists.

6. State Diagrams

The numerical results are summarized in the tableau shown in Fig. 8. The left column in this figure exhibits the stress distribution and the distribution of the $M+$ fraction across the bar at mid-length (element 51, integration point 1) at selected instants (23, 25, 30, 32, and 35 s). Note these diagrams employ separate ordinate axis: stresses refer to the left axis, while the $M+$ phase fraction refers to the right axis. The solutions obtained for the SMA material are plotted by symbols (stresses: diamonds, phase fractions: squares). Additionally, the first three diagrams (23, 25, and 30 s) on the left also incorporate reference stress solutions calculated for a hypothetical modified Prandtl-Reuss body which are indicated by solid lines (for details see Eq 8). The right column displays the bending moment diagrams along the bar axis at the same instants. The symbols used in these diagrams are explained in the following.

Various possibilities exist to assess the bending moment. For reference, ABAQUS provides data for the output variable "SM1." Further, the bending moment may be calculated on the basis of the knowledge of the stress and phase composition fields throughout the process. Generally, the bending moment $M(x)$ is an integral property of the bar defined by

$$M(x) = \int \sigma(x,z) \cdot z \, \mathrm{d}A \qquad \text{(Eq 5)}$$

where $\sigma(x, z)$ denotes the normal stress, being a function of the axial position x and the position in thickness direction z. For the discrete axial position at the bar mid-length, $\sigma(x, z)$ is plotted as function of z in Fig. 8 (left column). However, more insight is gained by employing the stress/strain relation of Eq 1 to incorporate the influence of the phase composition into that formula. In this case, the normal strain field $\varepsilon(x, z)$ must be determined additionally. According to the classical theory, this strain field is a linear function in the thickness coordinate z at any position x. Therefore, we employ the linear expression

$$\varepsilon(x,z) = m(x) \cdot z + n(x) \qquad \text{(Eq 6)}$$

where $m(x)$ indicates the bar curvature. The quantities $m(x)$ and $n(x)$ may be fitted to the linear strain profile provided by ABAQUS at any instant. Letting $(2 \cdot x_{M+} - 1) = \Delta X$ in Eq 4, the bending moment $M(x)$ can be computed as

$$\begin{aligned} M(x) &= \int \sigma(x,z) \cdot z \, \mathrm{d}A = \int E_M(\varepsilon(x,z) - \Delta X \cdot \varepsilon_\mathrm{T}) \cdot z \, \mathrm{d}A \\ &= E_M \cdot m(x) \cdot \int z^2 \, \mathrm{d}A + E_M \cdot n(x) \cdot \underbrace{\int z \, \mathrm{d}A}_{=0} - E_M \cdot \varepsilon_\mathrm{T} \\ &\quad \cdot \int \Delta X \cdot z \, \mathrm{d}A \\ &= E_M \cdot m(x) \cdot I_y - E_M \cdot \varepsilon_\mathrm{T} \cdot \int \Delta X \cdot z \, \mathrm{d}A \\ &= M_\mathrm{el}(x) - M_\mathrm{tr}(x) \end{aligned} \qquad \text{(Eq 7)}$$

wherein A denotes the cross-sectional area, I_y denotes the geometrical moment of inertia, and E_M is the Young's modulus as before. The resulting formula exhibits two contributions of the bending moment $M(x)$: $M_\mathrm{el}(x)$ represents the classical bending moment, which is valid for homogeneous phase composition if ΔX is independent of z. Therefore, this part represents the "elastic" contribution to the bending moment identical to the commonplace formula for bending of elastic beams. The second term $M_\mathrm{tr}(x)$ is missing in the classical theory. It represents the nonlinear contribution caused by phase transformation. This term vanishes if the phase composition is homogeneous over the cross section.

The diagrams in the right column in Fig. 8 exhibit these contributions to the bending moment, the resulting overall bending moment and the ABAQUS data. Here, hollow triangles indicate the elastic contribution $M_\mathrm{el}(x)$ and a solid black line the contribution of the phase transformation $M_\mathrm{tr}(x)$. Their difference according to Eq 7 is indicated by squares. These coincide perfectly with the ABAQUS data "SM1" indicated by black bullets.

After 23 s, the bar is in load stage II and experiences the lateral load causing a tensile load sufficient to initiate the transformation only in the outermost fibers SP1 and SP2. Apart from these, the remaining fibers are still linear-elastically loaded. Accordingly, the phase fraction of $M+$ exhibits small deviations from zero only for SP1 and SP2 at this instant. Consequently, the bending adheres to the classical solution as the transformation part is negligible.

The situation changes as more outer fibers gradually transform. After 25 s, SP1-SP12 are transforming at the tensile stress plateau (Fig. 8), whereas the stress beyond SP12 decays linearly. Note that the zero-point of the stress distribution has shifted off the geometric center. The distribution of the $M+$ fraction is linear in parts affected by the transformation. This inhomogeneity provokes a detectable contribution $M_\mathrm{tr}(x)$ to the overall bending moment visible in the right column of Fig. 8. Recall that Fig. 8 refers to the bar center where the imposed deflection is most pronounced. Towards the bar top and bottom, the deflection—and thus the stress—is insufficient to trigger any phase transformation, therefore $M_\mathrm{tr}(x)$ is zero in these parts. The elastic part $M_\mathrm{el}(x)$ and the transformation part $M_\mathrm{tr}(x)$ superimpose so as to produce the overall bending moment at this instant.

After 30 s (end of stage II), the lateral load has completely vanished. The stress distribution through the bar thickness (left column of Fig. 8, squares in Fig. 5) shows two linear branches. The left branch represents outer fibers which had previously experienced phase transformations (SP1-SP12) before they were slightly compressed by the relaxing inner fibers. The right branch refers to the remaining fibers (SP13-SP27). This situation provokes a bifurcation of the zero-stress location as discussed above and is clearly visible in the stress distribution at this instant. The phase composition is not affected by this process as the $M+$ fraction in the outer fibers remains stable between 25 and 30 s (elastic unloading in Fig. 5). The overall bending moment at this instant (right column) is very small but not zero, as the transformation part $M_\mathrm{tr}(x)$ and the elastic part are of the same order, but not identical. The resulting overall moment is sufficient to maintain a small remanent deflection.

Superimposing an axial load in stage III, the stress distribution in the outer fibers is squeezed towards the compressive stress plateau and the phase fraction changes in favor of $M-$. This process is exhibited by the stress and composition profiles in the left column of Fig. 8 (32 s). Accordingly, $M_\mathrm{tr}(x)$ is gradually reduced and eventually

eliminated once the bar has returned completely into the $M-$ phase, Fig. 8 (35 s).

The axial profile of the moment generated by ABAQUS (output quantity "SM1") is also well reproduced throughout stage II by the modified Prandtl-Reuss body (see Eq 8) and by a twofold integration of the lateral force $q(n, t)$ wherein the node number is converted to axial position (comparison not shown in Fig. 8 for perceptibility).

6.1 Comparison with a Prandtl-Reuss Body

Besides the numerical ABAQUS solution of the SMA bar, the upper three graphs in the left column of Fig. 8 exhibit additionally the spatial stress distributions within a bar made of a modified Prandtl-Reuss material under identical loading conditions. Prandtl-Reuss bodies represent a linear elastic—ideally plastic material which exhibits plastic yielding at the stress σ_0 according to the stress/strain relation

$$\frac{\sigma}{\sigma_0} = \frac{E \cdot \varepsilon/\sigma_0}{\left(1 + \left(\frac{E \cdot \varepsilon}{\sigma_0}\right)^n\right)^{1/n}}. \qquad \text{(Eq 8)}$$

The parameter n dictates the transition from the elastic branch to the stress horizontal. Its value was chosen as 10^4, ensuring a very distinct and sharp discontinuity. For comparison with the SMA material on the tension side, the elastic-plastic limit is shifted to the transformation strain of $-\varepsilon_T$ here, and σ_0 is identified with the SMA transformation stress. Clearly, this constitutive equation is applicable only in situations of quasiplastic yielding. In adherence with the SMA material elasticity is preserved for compressive stresses. This modified Prandtl-Reuss body produces the same stress distribution as the MAS model, see the solid lines in Fig. 8 at the instants of 23, 25, and 30 s. These curves coincide perfectly with the solutions obtained with the FEM/MAS model, hence giving additional evidence for the reliability of the MAS model.

7. Conclusions

The experimentally observed striking phenomenon of anti-buckling was analyzed by a FEM study which employs the Müller-Achenbach-Seelecke constitutive model for SMA. This model incorporates the calculation of the phase composition in these materials as internal variables through rate equations. The anti-buckling effect can be explained using this model as a sophisticated interplay of externally induced stress states and intrinsic stresses provoked by partial phase changes in the pseudo-plastic material regime. This interplay effects an asymmetric stress and phase distribution which is accompanied by bifurcation of the neutral fiber into two branches. The anti-buckling effect is caused by martensite-martensite transformations between generic twin variants $M+$ and $M-$ induced by axial loading which eliminates the bending moment instead of enforcing it like in classical plasticity. We were able to identify a contribution to the overall bending moment caused by the inhomogeneous phase composition. This analysis reproduces data at harmony with output obtained directly from ABAQUS. The MAS model result is verified by a modified elastic—ideally plastic constitutive law for situations where both models apply. In summary, we can safely state that the simulation presented here represents an example of successful application of the MAS model in the pseudo-plastic regime.

Acknowledgments

The authors wish to thank Professor S. Seelecke (Universität des Saarlandes, Saarbrücken, Germany) who has drawn our attention to the phenomenon of antibuckling. Dipl-Ing. S. Jaeger kindly helped in preparing the graphs. Financial support by the German Research Foundation (DFG) under Grant no. KA 2304/2-1 is highly appreciated.

Appendix

The spatial distribution of the stress and the $M+$ fraction are compiled in three-dimensional space in Fig. A1 for three instants. The state at the instant of maximum lateral load (25 s) is shown in Fig. A1(a), the one at the end of stage II (30 s) in Fig. A1(b) and (c) depicts the situation at 32 s (stage III) during the ongoing retransformation to $M-$. The data represent the following:

The data on the base plane and elevated above it towards the front represent the $M+$ fraction scaled to the equation $f = 3 + 16 \cdot \left(x_{M+} - \frac{1}{2}\right)$. The black lines connecting the outermost SP (SP1 in front and SP27 at the rear) for all elements illustrate the current geometrical configuration of the bar.

The more elevated black data points provide the stress $f = 10^{-8} \cdot \sigma/(1\ \text{Pa})$. The large gray dots highlight the location(s) of zero stress, i.e., the instantaneous location(s) of the neutral fiber(s).

The linear profile of the stress through the thickness in not transforming regions and the stress plateau in transforming sections is discernible. The stress plateau in Fig. A1(a) is apparent and spreads over the portion of the bar that was sufficiently strained to enter the transformation state on the tension side. At the bar center (element 51, integration point 1) SP1 to SP12 have entered this plateau, correlating with Fig. 3(a) to 5. As evident from Fig. 5, the stress plateau from the state of maximum lateral load is converted to a profile at the end of stage II (Fig. A1b) wherein the stress variation is larger the smaller is the SP index. The extremely rapid stress decline in the bar segments that had yielded before gives rise to a second neutral fiber over part of the bar length towards the end of stage II. Figure A1(a) and (b) reflects the stability of the phase fractions during lateral unloading.

The axial force in stage III affects a reduction of the curvature and forces the previously yielded segments (SP1-SP12 at the central element) to enter the stress plateau at the negative transformation stress. In Fig. A1(c), the five outer SP are currently transforming, correlating with Fig. 8(d) (left).

The top face reprints the stress-strain curve with full hysteresis (Fig. 2) scaled using the equations $\varepsilon = 0.1 + \frac{0.2}{50} \cdot \left(\frac{x}{1\ \text{mm}} - 50\right)$ and $\sigma = 2 \cdot 10^8 \cdot \left(\frac{z}{1\ \text{mm}} + 1.5\right)$ Pa to fit on the x- and z-axes. The superimposed gray points symbolize the spectrum of all prevailing stress-strain states present at the respective instant.

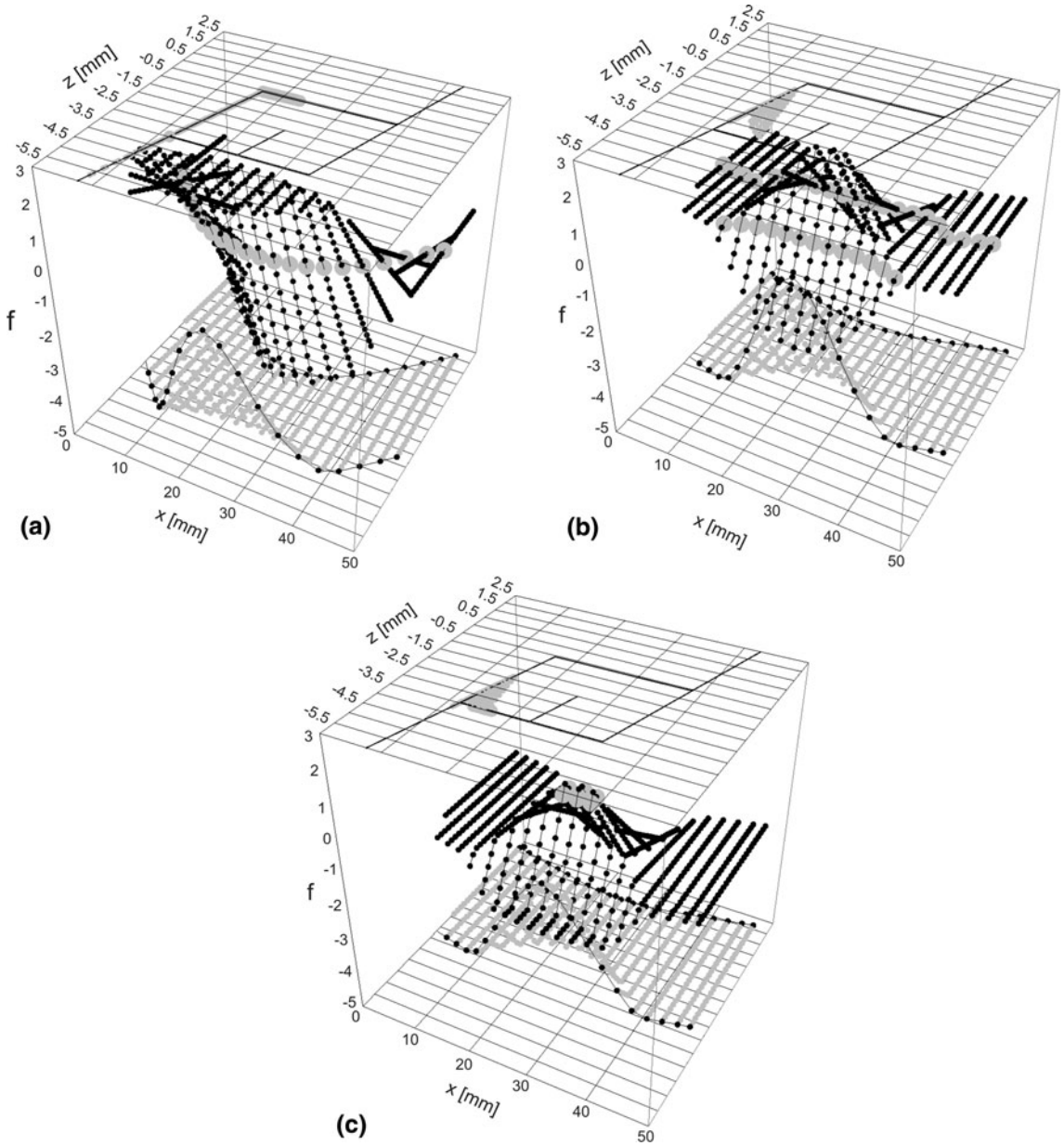

Fig. A1 Three-dimensional representation of the stress and *M*+ profile over the cross-section. (a) 25 s (maximum lateral load in stage II), (b) 30 s (end of stage II), (c) 32 s (stage III). Explanation of symbols see text

References

1. Y. Urushiyama, D. Lewinnek, J. Qiu, and J. Tani, Buckling of Shape Memory Alloy Columns (Buckling of Curved Column and Twinning Deformation Effect), *JSME (The Japan Society of Mechanical Engineers) Int. J. Ser. A, Solid Mech. Mater. Eng.*, 2003, **46**(1), p 60–67
2. Y. Urushiyama, Metallic Article Resistant to Buckling, U.S. Patent 6287399, publication date: 09/11/2001
3. I. Müller, A Model for a Body with Shape-Memory, *Arch. Ration. Mech. Anal.*, 1979, **70**(1), p 61–77
4. M. Achenbach and I. Müller, J. de Phys. Colloque C4, Suppl 12, 1982, **43**, p 163–167
5. M. Achenbach and I. Müller, Simulation of Material Behavior of Alloys with Shape Memory, *Arch. Mech.*, 1985, **37**, p 573–585
6. M. Achenbach, T. Atanackovic, and I. Müller, A Model for Memory Alloys in Plane Strain, *Int. J. Solids Struct.*, 1986, **22**(2), p 171–193
7. M. Achenbach, A Model for an Alloy with Shape Memory, *Int. J. Plast.*, 1989, **5**(4), p 371–395
8. M. Achenbach, "Simulation des Spannungs-Dehungs-Temperatur Verhalten von Legierungen mit Formerinnerungsvermögen," Dissertation, Technische Universität Berlin, Germany, 1987
9. S. Seelecke, Torsional Vibration of a Shape Memory Wire, *Cont. Mech. Therm.*, 1997, **9**, p 165–173
10. S. Seelecke and I. Müller, Thermodynamic Aspects of Shape Memory Alloys, *Math. Comp. Mod.*, 2001, **34**, p 1307–1355
11. S. Seelecke and I. Müller, Shape Memory Alloy Actuators in Smart Structures: Modeling and Simulation, *Appl. Mech. Rev.*, 2004, **57**(1), p 23–46
12. E. Hairer and G. Wanner, *Solving Ordinary Differential Equations II: Stiff and Differential-Algebraic Problems, Springer Series in Computational Mathematics*, Vol 14, 2nd ed., Springer, Berlin, 1996
13. Interactive webpage for the simulation of shape memory wires. www.smaterial.com
14. J.P. Frautschi, "Finite Element Simulations of Shape Memory Alloy Actuators in Adaptive Structures", M.Sc. Thesis, North Carolina State University, USA, 2003
15. Q. Li, "Modeling and Finite Element Analysis of Smart Materials", Ph.D. Thesis, North Carolina State University, USA, 2006

16. F. Richter, O. Kastner, and G. Eggeler, Implementation of the Muller-Achenbach-Seelecke Model for Shape Memory Alloys in ABAQUS, *J. Mat. Eng. Perf.*, 2009, **18**(5–6), p 626–630 (special issue containing contributions from the "Shape Memory and Superelastic Technology Conference", Stresa, Italy, September 21–25, 2008)
17. O. Heintze, O. Kastner, H. Sahota, and S. Seelecke, The role of thermomechanical coupling in the dynamic behavior of shape memory alloys, IUTAM Symposium on Smart Structures and Structronic Systems, *Proceedings of the IUTAM Symposium*, Magdeburg, Germany, September 26–29, 2000, U. Gabbert and H.S. Tzou, Ed., Springer, 2001, p. 145–152
18. F. Richter, Finite-Element-Simulations of Polycrystalline Shape Memory Alloys, *Smart Structures and Materials & Nondestructive Evaluation and Health Monitoring* 2008, San Diego, USA, March 09–13, 2008
19. F. Richter, O. Kastner, and G. Eggeler, *Finite—Element Model for Simulations of Fully Coupled Thermomechanical Processes in Shape Memory Alloys*, ESOMAT, Prague, September 2009
20. O. Heintze, "A Computationally Efficient Free Energy Model for Shape Memory Alloys—Experiments and theory", Ph.D. Thesis, North Carolina State University, USA, 2004
21. O. Heintze and S. Seelecke, A Coupled Thermomechanical Model for Shape Memory Alloys—From Single Crystal to Polycrystal, *Mater. Sci. Eng. A*, 2008, **481**–**482**, p 389–394
22. O. Kastner, F. Richter, and G. Eggeler, Multivariant Formulation of the Thermomechanically Coupled Müller-Achenbach-Seelecke-Model for Shape Memory Alloys, *ASME 2009 Conference on Smart Materials, Adaptive Structures and Intelligent Systems*, Oxnard, USA, September 21–23, 2009